Propulsive efficiency in drag-based locomotion of a reduced-size swimmer with various types of appendages

Asimina Kazakidi[a,*], Dimitris P. Tsakiris[b], John A. Ekaterinaris[c]

[a] *Department of Biomedical Engineering, University of Strathclyde, Glasgow, United Kingdom*

[b] *Institute of Computer Science, Foundation for Research & Technology-Hellas, Heraklion, Greece*

[c] *Department of Aerospace Engineering, Embry-Riddle Aeronautical University, Daytona Beach, USA*

Abstract

The propulsive efficiencies of multi-functional appendage configurations in a small drag-based swimmer are investigated computationally. Due to the lack of actual actuators to measure input power, efficiency is evaluated indirectly and may be instinctively associated to higher production of forward thrust. However, the relation is not intuitively self-evident, since the shape of the propulsive system is known to influence the generation of hydrodynamic forces, along with the particular kinematics used, which in turn affect the power consumption. The current article investigates this topic in the case of a reduced-size appendage-based swimmer producing small values of thrust, and discusses the role of design in the relation between propulsive efficiency and thrust production under a "sculling" kinematic motion profile. The study implements seven different shapes of appendages, inspired by both the biology and engineering, which perform a drag-based swimming pattern while being attached, in pairs, at the dorsal side of a common body. The work utilises an immersed boundary approach to solve numerically the fluid equations and capture the flow patterns around the swimmer. The results contribute to our understanding of drag-based propulsive systems and may influence the development of novel underwater robotic systems and limb prosthetic devices for underwater rehabilitation.

Keywords: Propulsive efficiency, drag-based swimming, immersed boundary method, numerical simulations, aquatic locomotion

1. Introduction

Swimming in nature has evolved from diverse aquatic morphologies, complex kinematic patterns, and distinctive mechanisms, such as body undulations, appendage motions, or jet production [1, 2]. Much like flying, the main objective of a swimming organism is to produce enough forward force (thrust) to overcome the induced resistive

*Corresponding Author
Email address: asimina.kazakidi@strath.ac.uk (Asimina Kazakidi)

force (drag), acting parallel to the direction of motion, and balance any lateral and vertical forces to avoid sinking [3]. The high density of water and its incompressibility makes swimming energetically easier than flying in an aerial medium, particularly for animals with a body density close to water density, which can remain suspended or cruise with minimal effort (neutral buoyancy). Other animals can regulate their buoyancy with alternate means and optimised energy consumption [4], or develop strategies that exploit vortices in the fluid to improve their swimming performances [5, 6, 7, 8].

In appendage-based swimming, propulsion can be achieved by the production of lift or drag, e.g. through flapping or through paddling or rowing, respectively, by moving the appendage(s) in an upward and downward cyclic fashion ("lift-based propulsion"), or parallel to the plane of motion ("drag-based propulsion"). The direction of the generated propulsive forces, namely whether they act perpendicularly or parallel to the plane of motion, has therefore played a significant role in the evolution of propulsive appendages. Nevertheless, the two modes can be interchangeably combined and the same appendages can be used equally for one or another mode, or in a mixed transitional fashion [9]. Lift-based propulsion has been associated with animals that can sustain higher attainted velocities for longer swimming durations, such as penguins, sea lions, sea turtles, sea butterflies, fish with lift-based pectoral fins (e.g. shiner seaperch), cartilagenous fishes, petropod molluscs, and certain species of crabs [1, 10]. Drag-based thrust, on the other hand, appears in animals that require the generation of sudden high-speed bursts for escaping, chasing, or high-speed maneuvering purposes, such as ducks, muskrats, freshwater turtles, angelfish, polychaete worms, water beetles, octopuses, shrimps, copepods, remipede crustaceans, and backswimmers [1, 10]. Drag-based paddling can be found also in quadrupedal mammals and human swimming.

Drag-based propulsion is superior for initial bursts of activity but, in general, the efficiency is low and the mode is considered evolutionary simpler than lift-based swimming [9]. Drag propulsors appear at various Reynolds numbers, though mostly work best at lower or intermediate values, where viscous effects can be exploited to contribute towards thrust production [11, 10]. Swimming based on drag forces is thus predominantly found in animals with mixed modes of locomotion, that is, animals that combine swimming with e.g. walking or burrowing modes (for example, ducks or polychaete worms), or animals that use their appendages for both propulsion and manipulation (multi-functional appendages, e.g. octopuses) [1]. Drag-based propulsion appears to work best at stationary systems, providing highest accelerations with a maximum attainted velocity, while thrust is reduced once the body is in motion. The easiest way therefore to examine morphological effects of appendages in drag-based systems is to maintain the body stationary.

The flow development and vortex generation around a drag-based swimming mode involving a periodic rotation of appendages can be very complex. The production of thrust is greatly affected by the morphology (shape or design) of the appendages and by their interaction with the main body (and its shape) on which they are attached [10, 12]. For example, streamlined appendages and bodies appear to be superior than non-streamlines shapes [9]. Engineering models on the labriform swimming mode, which is characteristic of the movement of paired pectoral fins and includes distinctive drag-based periodic power and recovery strokes, have shown that triangular fin designs surpass square or rectangular shapes in thrust production [13]. Delta-wing-shaped appendages also appear to generate stronger tip-vortex flow separation in a drag-based paddling

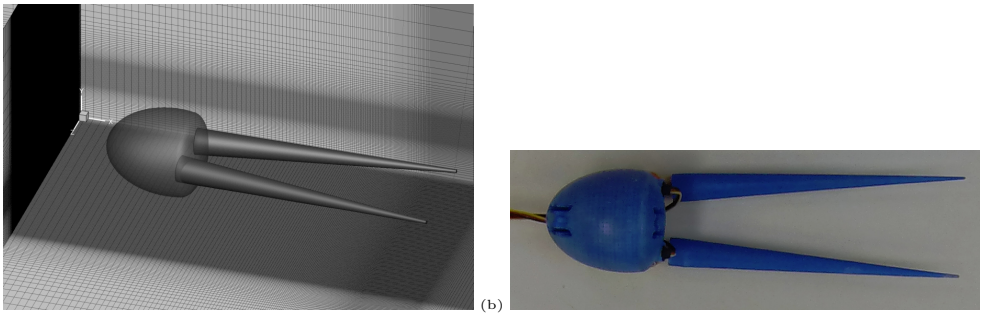

Figure 1: (a) Part of the computational domain used to simulate a small appedange-based swimmer, here shown with a pair of conical frustum appendages (Fig. 2a). (b) Robotic analogue (prototype, [16]).

mode [12]. The drag-based "sculling" mode, which includes a combination of a fast power stroke and a slow recovery stroke for thrust production [14, 15], equally presents interesting morphological dependences [16].

Expanding the work presented in [16], the current paper utilises a version of the four appendage morphologies presented and introduces three new designs, focusing on the evaluation of the propulsive efficiency in a small, slow swimmer with two appendages at the rear side (Fig. 1) and its relation to thrust production. This study contributes to the understanding of drag-based swimming modes and the influence of appendage morphology.

The rest of this paper is organized as follows: the drag-based swimming model is presented in Section 2; results on the propulsive efficiency and the role of appendage morphology in thrust production are highlighted and discussed in Section 3, and Section 4 concludes with some final remarks.

2. Computational Approach

The computational approach employed in this work to simulate propulsion of a small appendage-based aquatic swimmer is presented in this section. The numerical approach, also used in [17], is outlined first. The geometry representation and necessary details of the mesh are given next. The kinematics employed for the aquatic swimmer with the associated definition of the propulsive efficiency are then provided, before the presentation of results in the Section 3.

2.1. Numerical method

The flow around the swimmer is solved assuming the three-dimensional Navier-Stokes equations for incompressible Newtonian flow, expressed as:

$$\frac{\partial \mathbf{u}}{\partial t} + (\mathbf{u}\cdot\nabla)\mathbf{u} = -\frac{\mathbf{1}}{\rho}\nabla \mathrm{p} + \nu\nabla^{\mathbf{2}}\mathbf{u}, \qquad \nabla\cdot\mathbf{u} = \mathbf{0} \tag{1}$$

where $\mathbf{u}$ is the vector of velocity, p the pressure, ν the kinematic viscosity, and ρ the fluid density. The Reynolds number $Re = UD/\nu$, based on a circular appendage base diameter D (Fig. 2) and a fictitious mean steady-state forward speed U (explained in

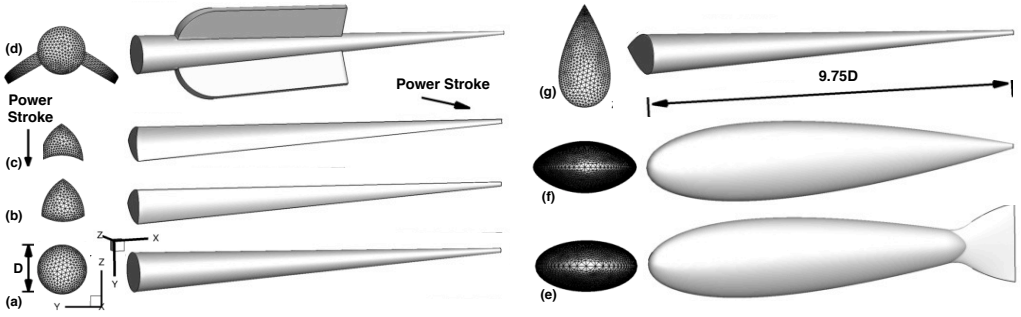

Figure 2: Shapes of appendages tested, in pairs, on a common body, as in Fig. 1: (a) Conical frustum, (b-c) Reuleaux shapes, (d) Flap-assisted conical frustum [16], (e-f) Fish-like with/without tail, (g) Airfoil-like. For each shape: (left) base with surface triangular mesh, (right) side viewpoint. Arrows in (c) indicate the direction of movement for all appendages, during the power stroke phase of the assumed kinematic profile.

Section 2.4), is approximately 340. The Strouhal number, expressed as $St = U/(WD)$, where W is the mean angular velocity (discussed in Section 2.3), is about 48.

The flow is numerically solved using a curvilinear/immersed boundary method, proposed by [18, 19]. Contrary to body-conforming methods, which include computationally demanding mesh deformation strategies, and based on the computationally inexpensive immersed boundary approach [20], the current hybrid method considers the swimmer's body and pair of appendages as sharp interfaces immersed in a fixed curvilinear computational domain. The position of the moving body is reconstructed with a 2nd-order quadratic interpolation scheme at the nodes near the interface between the fluid and the (solid) immersed boundaries. The nodes that correspond to the solid do not affect the solution of the fluid as they are identified separately. The advantage of this approach is its great flexibility in handling arbitrarily complex geometrical movements and deformations, while avoiding numerical instabilities and smearing effects around the immersed boundary. Further, the hybrid scheme does not require the explicit definition for the boundary conditions of the pressure field at the immersed boundary nodes. A second-order fractional step scheme is used for the implicit time integration of the flow equations. Validation of the method can be found in [18, 19] for several applications.

The CURVIB code is fully parallelized for massively parallel HPC systems and is not I/O intensive. The parallelization was performed using the PETSc library, which provides routines for parallel numerical solution of partial differential equations requiring the solution of sparse, large-scale nonlinear systems of equations. The background fluid mesh is parallelized by assigning a set of grid nodes to each processor using PETSc's distributed array (DA) object, which also manages parallel communications for structured mesh problems. The sparse parallel matrices and Krylov linear solvers in PETSc are used to solve the large sparse systems resulting from the discretization of momentum and pressure-correction equation. The implementation of the code is highly scalable for 3D flows, with an almost linear speedup for grids with 20 million nodes (scalability tests performed in several HPC clusters in USA and EU [17]), which are the typical sizes to be used in this study, and can utilise the openMPI implementation of MPI.

2.2. Geometry representation and mesh details

A small swimmer with an ellipsoid body and a pair of appendages on its dorsal surface (Fig. 1) is used here as a test platform for various appendage shapes (Fig. 2), with the aim to study their respective efficiency and thrust production. The body is designed to be $5D$ long in the major ellipsoid diameter and $3.25D$ wide in the minor diameter—where D is the base dimension of the conical appendage (Fig. 2a)—, while its dorsal side is shortened to 75% of the major dimension. The appendages are modelled at symmetrical (mirrored) positions behind the body and at 5° starting angle with the body axis. In the following, we present seven appendage geometries, of which a version of the first four, from (a) to (d), were presented first in [16] and the final three, from (e) to (g), are new.

(a) A conical frustum of $1D$ in base diameter, taper 9.75:1 (length to base diameter) and aspect ratio 17.5:1 (length to mean diameter, Fig. 2a).

(b-c) Two reuleaux-based shapes (Fig. 2b-c), with convex and concave sides with respect to the body axis, respectively, and base with circumcircle diameter of the reuleaux triangle D.

(d) A flap-assisted conical frustum, similar to (a) but with a pair of "flaps", positioned symmetrically at the sides of the appendage with respect to its axis and at 120° angle (Fig. 2d).

(e) A fish-like geometry with tail of elliptical cross-section (in the $yz-$direction), designed out of a NACA0010 airfoil shape, in the $xz-$direction, and a NACA0020 airfoil shape in the xy-direction. The tail has a height of $2D$ (Fig. 2e).

(f) A fish-like geometry without tail (Fig. 2f), of the same design specifications as (e).

(g) A frustum of a very thick airfoil with NACA0050 cross-section and taper 9.75:1.

These shapes are inspired both from biology, e.g. fish bodies or molluscs (octopus arms), or even loosely the human arm or leg (for the conical frustum), but also from engineering designs, e.g. the reuleaux shapes and airfoils. The study is non-exhaustive in the diversity of designs that could be used as engineered appendages, but rather it aims to examine certain distinct morphologies to highlight the association between thrust production and efficiency when they are used in pairs in such reduced-size drag-based swimmers. Single appendages have been previously examined in [15, 21]. In addition, the appendages are assumed to be rigid in this study. Effects of appendage deformation has been previously investigated in [17].

The computational domain is of size 30D x 15D x 30D in the xyz-directions respectively and is discretised in 20 million structured cuboid cells (Fig. 1a). A uniform finer mesh of 8D in x-, D in y-, and 2D in z-directions with element size h = 0.02D is constructed around the tips of the appendages to capture the flow separation. The grid resolution has been found sufficient for modelling viscous flow effects [17] and vortical wake structures near the swimmer. The swimmer is modelled in a quiescent fluid and each appendage is surface meshed with unstructured triangular elements (Fig. 2) of a total number of: (a) 38754 for the conical frustum, (b) 28776 and (c) 28608 for the reuleaux-based shapes, (d) 57338 for the flap-assisted conical frustum, (e) 49924 and (f) 16588 for the fish-like geometries, and (g) 50830 for the airfoil-like geometry.

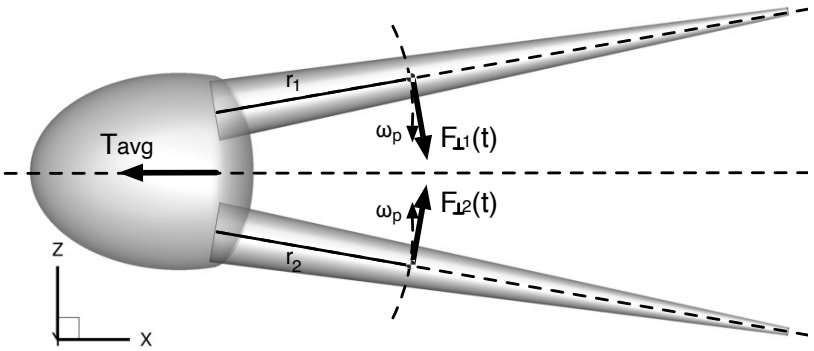

Figure 3: Schematic of applied force components during the power stroke for the calculation of the propulsive efficiency. T_{avg} is the average thrust over a cycle and $F_{\perp i}(t)r_i$ $(i = 1, 2)$ is the torque applied at the centre of mass of each appendage. See text for description.

2.3. Kinematics

The paired appendages follow kinematic profiles that are symmetrical to the body axis and are inspired from observations of a particular drag-based swimming mode, *sculling* [22, 23], which is observed for example in the octopus [24]. The simplified pattern is comprised of a high-thrust rapid motion of the appendages towards the body axis (*"power stroke"*) and a low-thrust, three-time slower, motion away from the body axis (*"recovery stroke"*). The angular velocity, $W(t)$, of each arm can be expressed as:

$$W(t) = \begin{cases} -2\omega_r \frac{t}{t_1} + 2\omega_r \frac{t^3}{t_1^3} - \omega_r \frac{t^4}{t_1^4}, & 0 \le t \le t_1; \\ -\omega_r, & t_1 < t \le T_r - t_1; \\ 2\omega_r \frac{t-T_r}{t_1} - 2\omega_r \frac{(t-T_r)^3}{t_1^3} - \omega_r \frac{(t-T_r)^4}{t_1^4}, & T_r - t_1 < t \le T_r; \\ 2\omega_r \frac{t-T_r}{t_1} - 2\omega_r^3 \frac{(t-T_r)^3}{\omega_p^2 t_1^3} + \omega_r^4 \frac{(t-T_r)^4}{\omega_p^3 t_1^4}, & T_r < t \le T_r + \beta t_1; \\ \omega_p, & T_r + \beta t_1 < t \le T_s - \beta t_1; \\ -2\omega_r \frac{t-T_s}{t_1} + 2\omega_r^3 \frac{(t-T_s)^3}{\omega_p^2 t_1^3} + \omega_r^4 \frac{(t-T_s)^4}{\omega_p^3 t_1^4}, & T_s - \beta t_1 < t \le T_s, \end{cases} \tag{2}$$

where $\omega_r = 10°/\,\mathrm{sec}$ represents the constant recovery stroke (low-thrust) angular velocity, $\omega_p = \beta\omega_r$ the power stroke (high-thrust) angular velocity, $\beta = 3$ the ratio between power and recovery strokes, $A = 5°$ the amplitude, and $\psi = 10°$ the angular axial position of the rotation. The overall cycle is assumed to be $T_s = T_r + T_p$, where $T_p = -\frac{3}{5\beta}(\beta^2+60)t_1$ corresponds to the power stroke and $T_r = \frac{61A}{30\omega}$ to the recovery stroke. Finally, $t_1 = \frac{A}{18\omega}$ is the time that $W(t)$ requires to reach the initial steady angular speed, for C^2 continuity. The swimmer's body is assumed stationary in the model, similar to typical robotic tests for force measurements, as the focus here lies on thrust generation by the paired motion of the appendages. An investigation of self-propulsion was previously presented in [15].

2.4. Propulsive efficiency

Propulsive efficiency (or Froude efficiency), η, is the ratio of the average output power, P_{out}, over the average input power, P_{in}, to a system ($\eta = P_{out}/P_{in}$) and, therefore, a measure of the gain versus loss of energy. In animal locomotion and engineering models, this is particularly interesting as it captures the effectiveness of a swimming mode over another. Here, the focus is on the influence of appendage morphology on drag-based swimming efficiency, under a common motion profile, and averaging is taken during one period of the cyclic appendage movement.

Although it is not straightforward to define the propulsive efficiency on a computational model swimmer that lacks power consumption from a real actuator and is restricted from self-propulsion, the propulsive efficiency η can be expressed as follows:

$$\eta = \frac{T_{avg}\ U}{\tau_{avg}\ W} \tag{3}$$

where T_{avg} is the average forward propulsive force (thrust) generated by each pair of appendages during one cycle and U is a fictitious mean steady-state forward speed that the swimmers would acquire as a result of the generated forward thrust (computed as the mean of the thrust integrals of each pair over the total mass of the system of two appendages [15], for all pairs). For rotational systems like the one examined here, P_{in} is the product of mean angular velocity W (calculated from Eq. 2) and total torque of the system, τ_{avg}, which can be expressed as:

$$\tau_{avg} = \sum_{i=1}^{2} F_{\perp i}\ r_i = (\sum_{i=1}^{2} m_i r_i^2)\dot{W} \tag{4}$$

where $F_{\perp i}$ $(i = 1, 2)$ represents the tangential force to each rotating appendage, respectively (Fig. 3), applied at the centre of mass, at length r_i from the centre of rotation, and $\dot{W}$ is the mean angular acceleration from $dW(t)/dt$. A mass m for each appendage was assumed, based on its volume and a constant density ρ representative of a neutral buoyant body in seawater. Since the system involves two identical appendages, Eq. 4 can be rewritten as: $\tau_{avg} = 2mr^2\dot{W}$.

3. Results and Discussion

This section presents and discusses results of flow simulation (Figs. 4, 5) in the wake of a small swimmer (Fig. 1) with the use of seven pairs of appendage designs (Fig. 2), undergoing a prescribed drag-based swimming motion (Eq. 2, for $\omega = 10°/\,\text{sec}$, $A = 5°$, $\beta = 3$, $\psi = 10°$). It also evaluates the produced thrust and propulsive efficiency of the swimmer (Figs. 6, 7) and attempts to find their correlation, as well as their dependences on other morphological and flow characteristics (Figs. 8, 9).

3.1. Flow perturbations

Assuming initially quiescent fluid and a stationary swimmer, the paired appendages move symmetrically, opening and closing together during the recovery (low-thrust) and

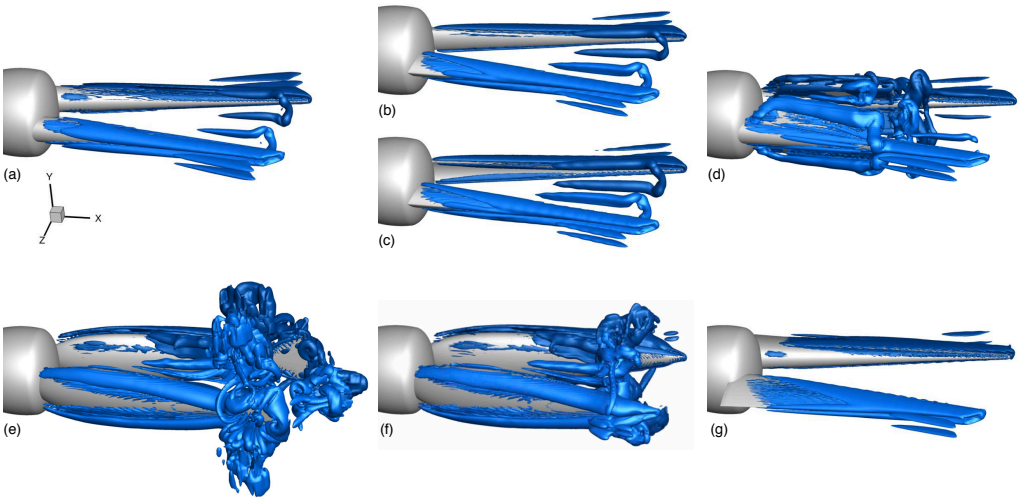

Figure 4: Instantaneous vortical flow patterns (based on iso-surfaces of the λ_2 criterion, $\lambda_2 = -1$) at the end of the high-thrust (power) stroke: (a) Conical frustum, (b-c) Reuleaux shapes, (d) Flap-assisted frustum [16], (e-f) Fish-like with/without tail, (g) Airfoil-like ($\omega = 10°/\,\mathrm{sec}$, $A = 5°$, $\beta = 3$, $\psi = 10°$).

power (high-thrust) strokes. Once time-periodicity is achieved, the flow-generated vortical structures in the near-wake region of the appendages can be observed at instantaneous snapshots during the cycle and are visualized with iso-surfaces of the λ_2 criterion [25] (λ_2=−1, Figs. 4, 5). The iso-surfaces detect the topology of the instantaneously-concentrated extent of the vortical flow and, as a result, the vortical cores. Figs. 4 and 5 examine such instantaneous patterns around the appendages at the end of the power and recovery strokes, respectively, of the kinematic motion profile.

The first three designs, namely the conical frustum and the two reuleaux shapes, are morphologically similar and display comparable vortical patterns, characterised by two main features: (i) Flow separated from the tip of each appendage, per stroke, extends rapidly into two counter-rotating vortices along the lee side of the appendage, merging with separated flow from the trailing face (Figs. 4a-c, 5a-c). (ii) The sudden move of the appendages inwards, during the power stroke, results in the forced detachment of these counter-rotating vortices from previous cycles (occurring mostly near the tip), which due to the low rate of diffusion in the surrounding fluid, they remain in the field and form horseshoe-like vortices.

These features can be discerned also in the flap-assisted conical frustum (Figs. 4d, 5d), however the tip-induced counter-rotating vortices extend only partially along the lee side, breaking symmetry at the point where flow is separated from the flaps. The horseshoe-like vortices are therefore diminished in strength and new complex vortical patterns fill the region between the two flaps. Flow disturbance is therefore much higher near the bases of the two appendages in the flap-assisted frustum, rather than near the tips, as previously seen in the simple frustum and reuleaux designs.

The two fish-like geometries, with and without a tail (Figs. 4e-f, 5e-f), cause clearly larger flow perturbations near the ends of the appendages, producing highly non-canonical

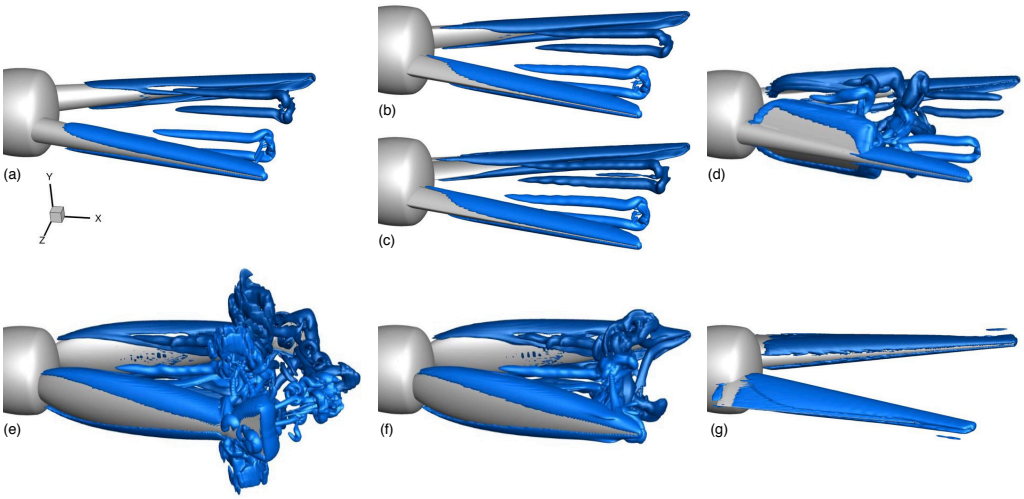

Figure 5: Instantaneous vortical flow patterns (based on λ_2 criterion, $\lambda_2 = -1$) at the end of the low-thrust (recovery) stroke: (a) Conical frustum, (b-c) Reuleaux shapes, (d) Flap-assisted conical frustum [16], (e-f) Fish-like with/without tail, (g) Airfoil-like ($\omega = 10°/\,\text{sec}$, $A = 5°$, $\beta = 3$, $\psi = 10°$)

vortical structures that extend into the surrounding three-dimensional fluid space, during both strokes. Separation of flow along the entire length of each appendage is evident and is stronger during the power stroke.

Due to the small amplitude of the motion and, hence, small incidence angles of the appendages with the flow, the airfoil-like design has the least impact on the surrounding fluid (Figs. 4g, 5g), though flow separates along the length of the appendages.

3.2. Hydrodynamic performance (thrust and efficiency)

The hydrodynamic performance of the presented swimmer can be assessed through the analysis of the produced thrust, T, and propulsive efficiency, η, for each pair of appendages. Figure 6a presents the temporal variation of the thrust coefficient, C_T, that is, of the hydrodynamic forward force that acts on the swimmer, along the direction of swimming, as a result of appendage motion. C_T is a non-dimensional parameter and is calculated as $T/0.5\rho U^2 A_{proj}$ [15], where A_{proj} is the projected area for each shape.

As indicated from the analysis of the vortical patterns in the near-wake region around the appendages (Section 3.1), the fish-like geometries appear to produce the highest peak thrust values (black and orange lines in Figs. 6a), with the tail adding a considerable extra propulsive component to the system. The flap-assisted conical frustum (green line, Fig. 6a) also produces high peak values, but the conical frustum, reuleaux and airfoil-like shapes generate more moderate peak forces. It appears, therefore, that increasing the induced perturbations in the flow, due to increased flow separation and complex vortical structures, increases the generated peak thrust. However, in average numbers the trend is less straightforward. Appendage *(d)*, the flap-assisted frustum (Fig. 6b), presents the highest average thrust coefficient, with shape (e), the fish-like with tail, coming second and the one without tail (shape *(g)*) showing a smaller average C_T value than shape *(c)* and almost equal to *(b)*. A linear fit can only poorly estimate peak C_T being roughly 60

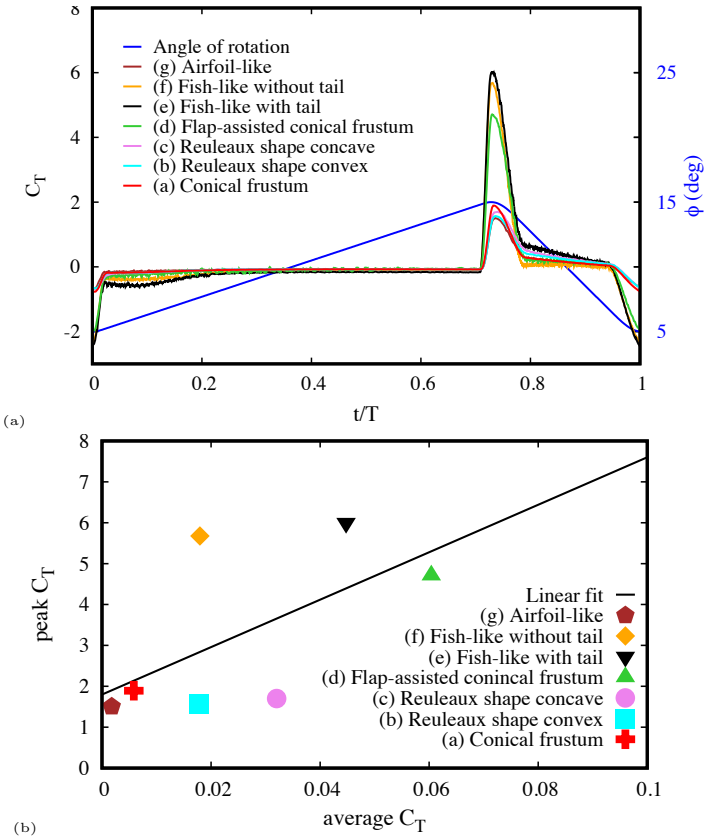

Figure 6: (a) Temporal variation of the propulsive thrust coefficient, C_T once time periodic response has been achieved. (c) Comparison between peak and average values. ($\omega = 10°/\,\mathrm{sec}$, $A = 5°$, $\beta = 3$, $\psi = 10°$).

times larger than the average values; rather, the graph indicates that designs causing large disturbances in the flow (shapes *(d)-(f)*) can produce more moderate-to-higher average C_T values (and clearly larger peak values) than designs resulting in less perturbations and display more moderate-to-lower C_T (and lower peak values).

To understand better the role of appendage morphology on the performance of the swimmer, the propulsive efficiency, η, is calculated as described in Section 2.4 and shown in Fig. 7a for each appendage. The flap-assisted geometry (shape *(d)*) exhibits the highest efficiency, since the power consumption is smallest and most of the average input power, P_{in}, is used to generate thrust (Fig. 7b). (Note that the same shape produces the highest average C_T, Fig. 6b). The second-highest efficiency design is the reuleux concave, which also displays surprisingly low power consumption, as compared with shapes *(a)* and *(b)*, yet with the lowest value of input power. (Note that this geometry presented the highest average C_T from the group of geometries that cause small flow perturbations). In fact, the reuleux concave surpasses in efficiency both fish-like geometries, of which the large peak thrust values and highly-complex induced vortical flow perturbations appear to come at the expense of considerable power consumption. The remaining three designs

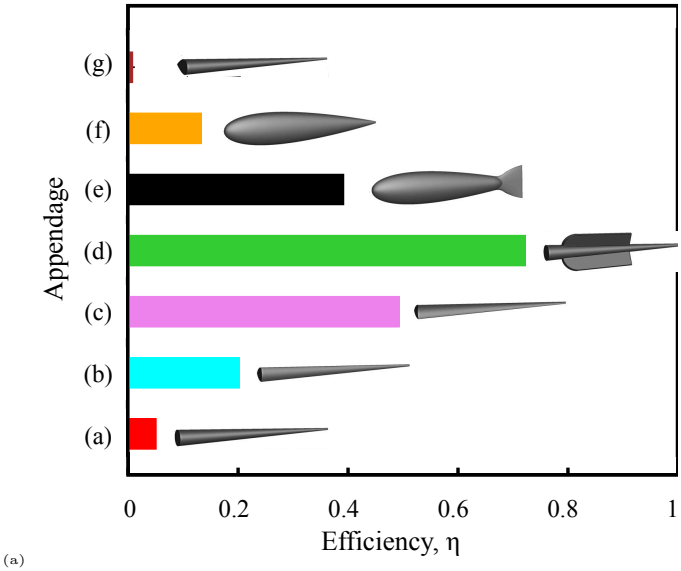

(a)

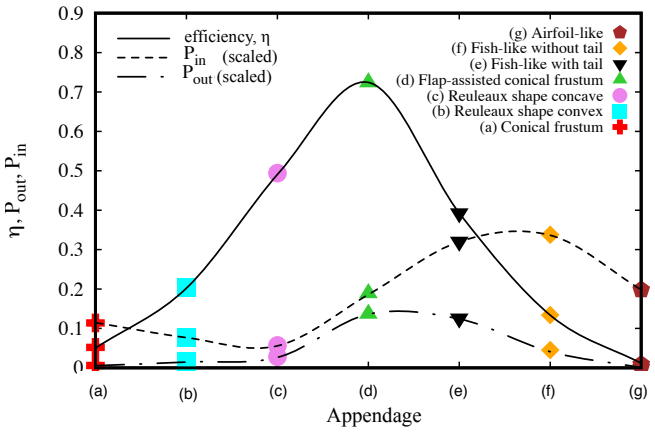

(b)

Figure 7: (a) Evaluation of the propulsive efficiency, η, for the swimmer, calculated according to Eq. 3 for each pair of appendages. (b) Efficiency η and output P_{out}, input P_{in} power (scaled) for each pair.

exhibit similar or smaller efficiencies.

Figures 8a-d examine the correlations of the propulsive efficiency, η, with several morphological and fluid characteristics, in particular the average thrust coefficient, C_T (Fig. 8a), the normalised mean forward speed U_n (normalisation by U, Fig. 8b), the
260 normalised total mass of the system of two appendages (based on the total average, Fig. 8c), and the normalised projected area (based on the total average, Fig. 8d).

Overall, the efficiency appears to have a strong, almost linear, relationship with the thrust coefficient, being approximately 12 times larger (Fig. 8a). Individual appendages, nevertheless, are more loosely linked. For example, the fish-like appendage with tail has

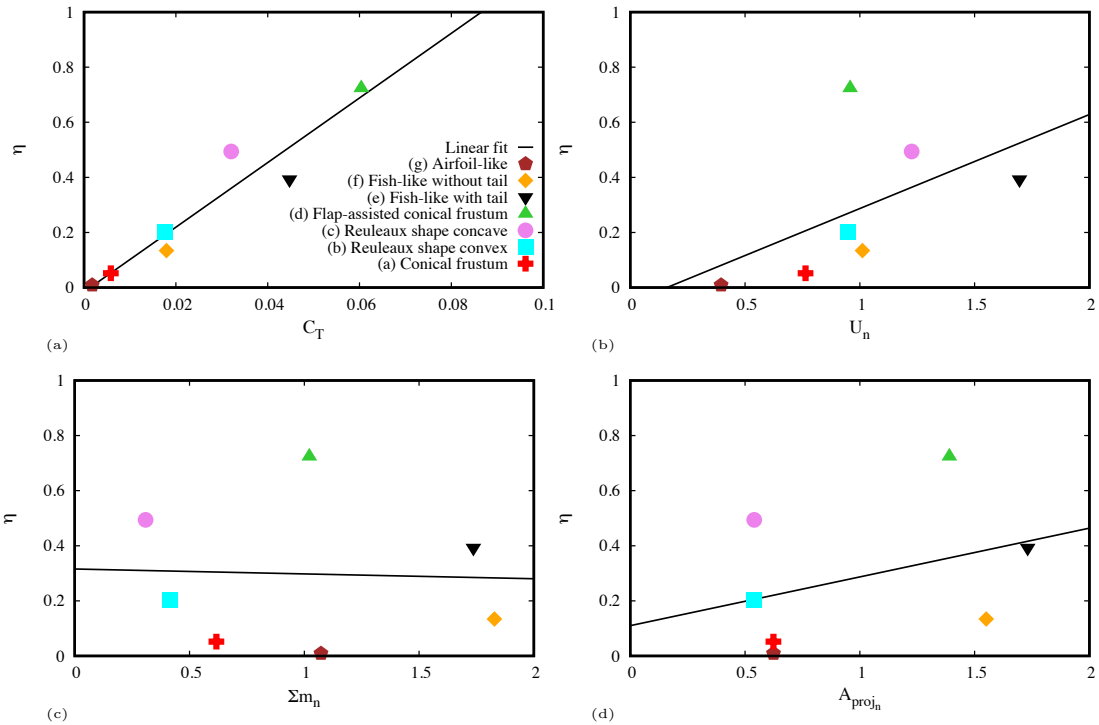

Figure 8: Propulsive efficiency, η (Eq. 3) plotted against the (a) average thrust coefficient C_T, (b) normalised mean forward speed U_n, (c) normalised total mass Σm_n, (d) normalised projected area A_{proj_n}.

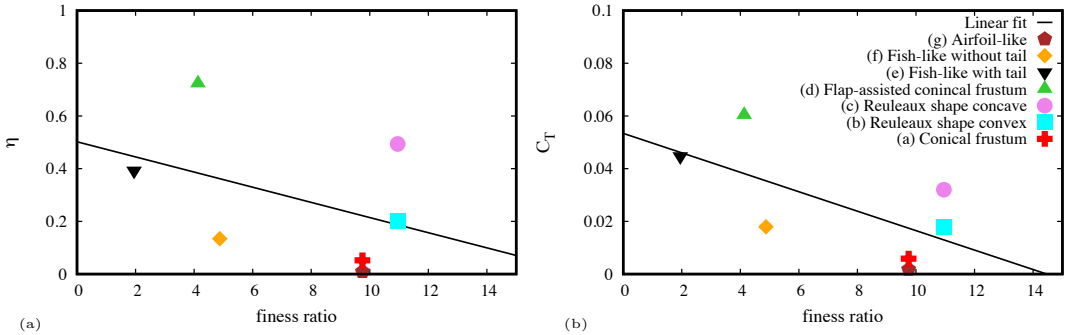

Figure 9: (a) Propulsive efficiency, η (Eq. 3), and (b) average thrust coefficient, C_T, as a function of the fineness ratio, FR.

higher C_T but lower η than the reuleux concave, which falls above the line fit. The flap-assisted conical shape displays the highest efficiency for the highest average thrust, despite having a peak value that is lower than the fish-like shapes (as seen earlier in Fig. 6). The other four geometries have all lower values in both C_T and η.

The relationship between efficiency and normalised mean forward speed, U_n, is less evident (Fig. 8b). A poor linear fit gives a ratio of approximately 0.3 between the two, but the plot demonstrates that the three highest-efficiency appendages (flap-assisted, reuleux concave and fish-like with tail) produce moderate-to-high speeds, whereas low-efficiency appendages (shapes *(a), (b), (f)* and *(g)*) produce moderate-to-low forward speeds.

Figure 8c indicates that η has a small depedence on the normalised total mass of the system, with both high-efficiency and low-efficiency shapes having a wide range of mass values. The plot of the efficiency η over the normalised projected area, A_{proj_n} (Fig. 8d) shows a moderate influence, however it highlights that both large and small geometries, (based on the projected areas) can have equally low and high efficiencies.

Finally, in Fig. 9 the efficiency and thrust coefficient for each shape are evaluated based on the Finess Ratio (FR), a ratio defined as the overall appendage length to maximum width, which according to [9] could be used as an index to associate design with propulsive performance. Since all appendage shapes have the same overall length, $9.75D$ in the $x-$direction (as shown in Figs. 1, 2), the FR depends only on the maximum width (thickness). Both η and C_T in Fig. 9 display an inverse relation to FR, with the highest thrust production appendages having smaller FR values for a range of η and C_T numbers. A similar relationship between drag coefficient and FR has been previously found in [1].

4. Conclusions

In this paper, the propulsive efficiency and thrust production of various appendage morphologies in a reduced-size swimmer are investigated with the use of immersed-boundary computational fluid dynamics methods. The shape of appendages is found to influence both mean thrust production and efficiency, but these have no direct causative correlation with the extent of flow perturbations in the surrounding fluid medium, induced during the prescribed periodic motion. In fact, it is found that appendages that result in extended tip-vortex flow separation and complex vortical structures (fish-like shapes) produce less average thrust and are less efficient than appendages that induce flow disturbances in regions closer to their bases (flap-assisted conical frustum).

The results further demonstrate that the most efficient propulsion for the swimmer examined corresponds to the morphology with flaps. They also highlight that although, on average, the efficiency appears to be linearly correlated with thrust production, individual appendages may not necessarily be; for example, higher-thrust morphologies (e.g. fish-like with tail) may be less efficient than lower-thrust morphologies (e.g. reuleux concave). Design needs, therefore, to consider energetic efficiency, in addition to produced thrust. Future investigations will attempt to include appendages related to prosthetic devices for underwater rehabilitation.

5. Acknowledgments

The authors would like to thank F. Sotiropoulos and D. Angelidis for providing the CURVIB code, and M. Sfakiotakis, A. Chatzidaki, T. Evdaimon for their assistance with the robotic studies. We acknowledge that the results of this research have been achieved using the H2020 PRACE-4IP DECI-13 resources (ICARUS project, 13DECI0256) on Beskow cluster based at KTH Royal Institute of Technology.

6. Funding

This work was supported, in part, from the European Union?s Horizon 2020 research and innovation programme under the Marie Sk?odowska-Curie grant agreement No 749185 (A.K.) and by the project "Advanced Research Activities in Biomedical and Agro alimentary Technologies" (MIS 5002469) implemented under the "Action for the Strategic Development on the Research and Technological Sector" (D.P.T.), funded by the Operational Programme "Competitiveness, Entrepreneurship and Innovation" (NSRF 2014-2020) and co-financed by Greece and the European Union (European Regional Development Fund).)

References

[1] S. Vogel, Life in Moving Fluids: The Physical Biology of Flow, Princeton University Press, 1994.

[2] F. Fish, Comparative kinematics and hydrodynamics of odontocete cetaceans: Morphological and ecological correlates with swimming performance, J. Exp. Biol. 201 (1998) 2867—2877.

[3] M. Sfakiotakis, D. Lane, J. Davies, Review of fish swimming modes for aquatic locomotion, *IEEE J. Ocean Eng.* **24** (2) (1999) 237–252.

[4] R. Alexander, Size, speed and buoyancy adaptations in aquatic animals, *Amer. Zool.* **30** (1990) 189–196.

[5] G. Lauder, E. Drucker, Forces, fishes, and fluids: Hydrodynamic mechanisms of aquatic locomotion, *News Physiol. Sci.* **17** (2002) 235–240.

[6] J. Liao, D. Beal, G. Lauder, M. Triantafyllou, Fish exploiting vortices decrease muscle activity, *Science* **302** (2003) 1566–1569.

[7] J. Dabiri, S. Colin, J. Costello, Fast-swimming hydromedusae exploit velar kinematics to form an optimal vortex wake, *J. Exp. Biol.* **209** (2006) 2025–2033.

[8] I. Bartol, P. Krueger, J. Thompson, W. Stewart, Swimming dynamics and propulsive efficiency of squids throughout ontogeny, *Integr. Comp. Biol.* **48** (6) (2008) 720–733.

[9] F. Fish, Transitions from drag-based to lift-based propulsion in mammalian swimming, Amer. Zool. 36 (1996) 628–641.

[10] J. Walker, Functional morphology and virtual models: Physical constraints on the design of oscillating wings, fins, legs, and feet at intermediate reynolds numbers, Integr. Comp. Biol. 42 (2002) 232—242.

[11] J. Walker, M. W. Westneat, Mechanical performance of aquatic rowing and flying, Proc. R. Soc. Lond. B 267 (2000) 1875–1881.

[12] D. Kim, M. Gharib, Characteristics of vortex formation and thrust performance in drag-based paddling propulsion, J. Exp. Biol. 214 (2011) 2283–2291.

[13] R. Blake, Influence of pectoral fm shape on thrust and drag in labriform locomotion, J. Zoo. Lond. 194 (1981) 53–66.

[14] M. Sfakiotakis, A. Kazakidi, N. Pateromichelakis, J.A. Ekaterinaris, D.P. Tsakiris, Robotic underwater propulsion inspired by the octopus multi-arm swimming, in: IEEE Int Conf Rob Autom (ICRA), St. Paul, USA, 2012, pp. 3833–3839.

[15] A. Kazakidi, V. Vavourakis, D. P. Tsakiris, J. Ekaterinaris, A numerical investigation of flow around octopus-like arms: near-wake vortex patterns and force development, Comp Meth Biomech Biomed Eng 18 (12) (2015) 1321–1339.

[16] A. Kazakidi, D. P. Tsakiris, J. A. Ekaterinaris, Impact of arm morphology on the hydrodynamic behavior of a two-arm robotic marine vehicle, IFAC PapersOnLine 50 (1) (2017) 2304 – 2309.

[17] A. Kazakidi, D. P. Tsakiris, D. Angelidis, F. Sotiropoulos, J. A. Ekaterinaris, CFD study of aquatic thrust generation by an octopus-like arm under prescribed deformations, Comput & Fluids 115 (2015) 54–65.

[18] A. Gilmanov, F. Sotiropoulos, A hybrid cartesian/immersed boundary method for simulating flows with 3d, geometrically complex, moving bodies, J Comp Phys 207 (2005) 457–492.

[19] L. Ge, F. Sotiropoulos, A numerical method for solving the 3d unsteady incompressible navier–stokes equations in curvilinear domains with complex immersed boundaries, J Comput Phys 225 (2007) 1782–1809.

[20] C. Peskin, Flow pattern around heart valves: a numerical method, J Comput Phys 10 (1972) 252–271.

[21] A. Kazakidi, V. Vavourakis, N. Pateromichelakis, J.A. Ekaterinaris, D.P. Tsakiris, Hydrodynamic analysis of octopus-like robotic arms, IEEE Int Conf Rob Autom (ICRA) (2012) 5295–5300. St. Paul, USA.

[22] M. Sfakiotakis, A. Kazakidi, N. Pateromichelakis, D.P. Tsakiris, Octopus-inspired 8-arm robotic swimming by sculling movements, in: IEEE Int Conf Rob Autom (ICRA), Karlsruhe, Germany, 2013, pp. 5135–5141.

[23] M. Sfakiotakis, A. Kazakidi, D. P. Tsakiris, Octopus-inspired multi-arm robotic swimming, Bioinsp Biomim 10 (3) (2015) 035005.

[24] A. Kazakidi, X. Zabulis, D. P. Tsakiris, Vision-based 3d motion reconstruction of octopus arm swimming and comparison with an 8-arm underwater robot, in: IEEE Int Conf Rob Autom (ICRA), Seattle, WA, USA, 2015, pp. 1178–1183.

[25] J. Jeong, F. Hussain, On the identification of a vortex, J Fluid Mech 285 (1995) 69–94.